



HAL
open science

Noise Robust Mojette Reconstructions for Missing Wedge Effect Attenuation

Benoît Recur, Pascal Desbarats, Jean-Philippe Domenger

► **To cite this version:**

Benoît Recur, Pascal Desbarats, Jean-Philippe Domenger. Noise Robust Mojette Reconstructions for Missing Wedge Effect Attenuation. *Journal of Multimedia Processing and Technologies*, 2010, 1 (4), pp.208-227. hal-00627493

HAL Id: hal-00627493

<https://hal.science/hal-00627493>

Submitted on 28 Sep 2011

HAL is a multi-disciplinary open access archive for the deposit and dissemination of scientific research documents, whether they are published or not. The documents may come from teaching and research institutions in France or abroad, or from public or private research centers.

L'archive ouverte pluridisciplinaire **HAL**, est destinée au dépôt et à la diffusion de documents scientifiques de niveau recherche, publiés ou non, émanant des établissements d'enseignement et de recherche français ou étrangers, des laboratoires publics ou privés.

Noise Robust Mojette Reconstructions for Missing Wedge Effect Attenuation

B. Recur, P. Desbarats, and J.P. Domenger

LaBRI, Bordeaux 1 University

351 cours de la Libération 33400 Talence, France

e-mail: brecur@labri.fr, desbarats@labri.fr, domenger@labri.fr

Abstract— The Mojette transform is a tomographic reconstruction method based on a discrete and finite interpretation of the Radon theorem. Since the Mojette acquisition follows the discrete image geometry, this method resolves the well-known irregular sampling problem. A specific algorithm called Corner Based Inversion (CBI) is proposed to reconstruct without any error an image from its projections even if the angular coverage is not sufficient (missing wedge). However, this reconstruction is noise sensitive and reconstruction from corrupted data fails. In this paper, we develop new noise robust CBI algorithms and we apply them both on discrete Mojette acquisitions and on usual Radon acquisitions. Reconstruction results are discussed to highlight the efficiency of these algorithms for usual tomography and perspectives are proposed to reduce the missing wedge effect.

*Keywords—*Mojette transform, Corner Based Inversion, noisy projections, missing wedge effect.

1 Introduction

X-Rays form an electromagnetic wave which has a wavelength much shorter than visible light. This property allows it to go through matter. In this process, the X-Ray beam undergoes an attenuation proportional to the density of the traversed matter. It is the basic principle for X-Ray radiography. In medical or industrial CT scanner, a 2D slice of the imaged object is acquired by casting X-Rays following several angles around the object. For each angle, the attenuation of the X-Ray beam is measured leading to a 1D projection of the object. The 2D slice is then reconstructed from a set of projections [10] using the Radon theorem [12]. The main drawback of this method is that the Radon theorem is defined in the continuous domain whereas images are in the discrete domain. The continuous-to-discrete mapping leads to approximations or deformations, especially when a set of successive projections is not available (i.e. missing wedge effect [2]).

Different approaches can be followed to overcome these problems or to reduce their effects. The first one is to try to improve reconstructed image quality by filtering in the frequency domain or by reconstructing with multiscale and/or iterative methods. The second one is to directly implement discrete reconstructions because they are not sensitive to the missing wedge effect.

In this article, we first introduce the Radon theorem and the discrete Mojette Transform [6]. Second, the Corner Based Inversion (CBI) is defined as an efficient and exact reconstruction. It is not sensitive to the missing wedge effect but noise sensitivity is the main limitation of this inversion.

Consequently, we develop and optimize new CBI algorithms to attenuate the noise effect and to reconstruct an image from noisy Mojette projections. Afterwards, a reconstruction from a Spline Mojette acquisition is proposed. The results are discussed and compared with other usual Mojette reconstructions (which are not noise sensitive but also not robust to the missing wedge). Then, we explain how Spline Mojette is equivalent to a specific discrete

Radon transform and we detail how the overall proposed algorithms can be used in usual tomography. Finally, a preliminary study to reduce the missing wedge effect by using the new methods is investigated.

2 Material and Methods

2.1 Radon Transform

The Radon transform \mathcal{R} maps a 2D function f into a 1D projection for a given angle θ and a module ρ [12], [18]. This transform is defined by :

$$\mathcal{R}_\theta(\rho) = \int_{-\infty}^{\infty} \int_{-\infty}^{\infty} f(x, y) \delta(\rho - x \cos \theta - y \sin \theta) dx dy \quad (1)$$

where θ and ρ are respectively the angular and radial coordinates of the projection line (θ, ρ) , and $\delta(\cdot)$ is the Dirac impulse function. The sinogram denoted \mathcal{S} is made of a set of projection lines. Each projection line corresponds to an acquisition using equation 1.

From an image I sized $W \times H$, the discrete Radon transform R is [18]:

$$R_\theta(\rho) = \sum_{-\infty}^{\infty} \sum_{-\infty}^{\infty} I(i, j) \alpha_{ij\theta\rho} \quad (2)$$

where the pixel kernel $\alpha_{ij\theta\rho}$ defines the weight value between a pixel (i, j) and a projection line (θ, ρ) . It is usually the discrete Dirac impulse or the order-0 spline kernel (which considers a projection proportionally to the distance crossed into the pixel) [19], [20]. A discrete acquisition is achieved according to a constant radial sampling step $\delta\rho$ and a constant angular sampling step $\delta\theta$.

The inverse Radon transform recovers the original domain from the projections. From a sinogram \mathcal{S} sized $N_\theta \times N_\rho$, the discrete inverse Radon transform R^{-1} is :

$$R^{-1}(i, j) = I(i, j) = \sum_{i_\theta=1}^{N_\theta} \sum_{i_\rho=1}^{N_\rho} \mathcal{S}(i_\theta, i_\rho) \alpha_{ij\theta\rho} \quad (3)$$

where i_θ and i_ρ are respectively the angular and radial indexes of the projection line (θ, ρ) in the sinogram and $\mathcal{S}(i_\theta, i_\rho) = \mathcal{R}_\theta(\rho)$.

The Radon transform and its inverse are exact in continuous domain. In computerized tomography, we have to use its discrete inversion (equation 3) to compute a discrete image. The used sinogram can be given from a continuous (equation 1) as well as a discrete (equation 2) acquisition. However, this discretization induces approximations on the reconstructed image. Well-known algorithms have been developed for the last decades to increase the quality of resulted images. Note for instance the back-projection of filtered projections (BFP), reconstructions in Fourier space [16] and iterative methods based on the algebraic techniques [4], [9], [5] or maximum likelihood [3], [17], [11].

For instance, the sinogram 1(b) is acquired following several angles and samples from the original domain 1(a). Each sinogram column represents the sample values of each projection. From this sinogram, an image imaging the original domain is computed by using the BFP [18] (figure 2(a)) or the iterative SART [1] algorithm (figure 2(b)).



Figure 1. (a) Original domain. (b) Acquisition of the original domain following 90 angles (X-axis) of 64 samples (Y-axis).



Figure 2. Images reconstructed with the BFP (a) and the SART (b) algorithms using the sinogram 1(b).

2.2 Limitations of the Radon Transform

These methods suffer from two main limitations. They follow a fixed acquisition geometry (the angular and radial steps are constant). So, an irregular sampling appears between pixels and projections because the discrete image properties are not taken into account for the acquisition. Moreover, the reconstructed image is considered globally and not one pixel after the other. Since the already reconstructed pixels are not deduced on the projections, the sinogram always contains all the data instead of the strictly necessary data for not yet reconstructed pixels.

The global deformation of the regions in the reconstructed images (figure 3) are due to the missing wedge effect. It appears when the acquired sinogram angles do not cover all the directions between 0 and π . For instance, the sinogram shown on the figure 3(a) only contains projections acquired between 0 and $\frac{2}{3}\pi$. The successive missing angles between $\frac{2}{3}\pi$ and π are expressed by the black columns. With such a sinogram, methods based on the Radon theorem (BFP 3(b) and algebraic SART method 3(c) results) suffer from deformations.

2.3 Mojette Transform

The Dirac-Mojette transform [8], [7], [6] is defined as a discrete version of the Radon transform. It considers only angles $\theta = \tan^{-1}\left(\frac{q}{p}\right)$ where $p \in \mathbb{Z}$ and $q \in \mathbb{Z}^+$ are relatively prime and are respectively the number of pixel displacement horizontally and vertically. The Dirac-Mojette transform is so given

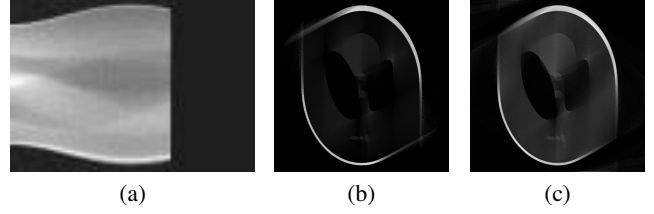


Figure 3. Radon acquisition (a) with a $\frac{\pi}{3}$ missing wedge. BFP (b) and algebraic SART method (c) reconstructions.

by (Equation 4) :

$$M_{p,q}(b) = \sum_{-\infty}^{+\infty} \sum_{-\infty}^{+\infty} I(i, j) \Delta(b - ip + jq) \quad (4)$$

Therefore, the transformed domain consists in projections where each element $M_{p,q}(b)$, called a bin, is the sum of every pixel intersecting the line $b = ip - jq$. The Dirac-Mojette transform result is described in figure 4 for a 3×3 image and for the set of projections $\{(-1, 1), (1, 1), (1, 0)\}$.

The geometry of the Dirac-Mojette sinogram is defined by p and q . The number of bins on the projection (p, q) is (for a $W \times H$ image) [15] :

$$N_{p,q}(p, q) = (W - 1)|p| + (H - 1)|q| + 1 \quad (5)$$

Moreover, note that the angular and radial steps are not yet constant and depend on the chosen projection set. For instance, the step between each bin line on the projection (p, q) is :

$$d_{\rho} = \frac{1}{\sqrt{p^2 + q^2}} \quad (6)$$

This geometry solves the Radon sampling problem because sampling properties are defined and adjusted for each projection angles. It results that each pixel contributes to one and only one bin value per projection.

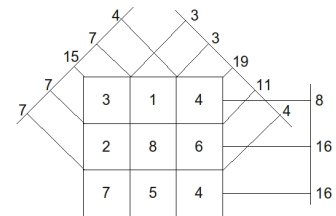


Figure 4. Result of the Mojette transform on a 3×3 image and for the set of projections $\{(-1, 1), (1, 1), (1, 0)\}$.

An image can be recovered if the set of projections follows the Katz criterion [10]. It ensures that the image is reconstructed by the set of projections $P = \{(p_i, q_i), p_i \in \mathbb{Z}, q_i \in \mathbb{Z}^+, i \in 1 \dots N\}$ if :

$$W \leq \sum_{i=1}^N |p_i| \text{ or } H \leq \sum_{i=1}^N |q_i| \quad (7)$$

The set of projections P can be computed automatically with the Farey series [15].

The inverse transform back-projects the bins of the different projections onto the reconstructed image. A single bin-pixel correspondence must be determined to reconstruct a pixel [8]. We use the specific acquisition denoted $M_{p,q}^t(b)$ done from an image where each pixel is valued 1. $M_{p,q}^t(b)$ is the pixel number to reconstruct on the bin (b, p, q) . If $M_{p,q}^t(b) = 1$, there is only one pixel (i, j) on the bin whose value becomes $I(i, j) = M_{p,q}(b)$. Its value is subtracted from each projection $M_{p_l, q_l}(b_l)$ where it appears and corresponding $M_{p_l, q_l}^t(b_l)$ are decremented. A step of this algorithm is shown on the figure 5.

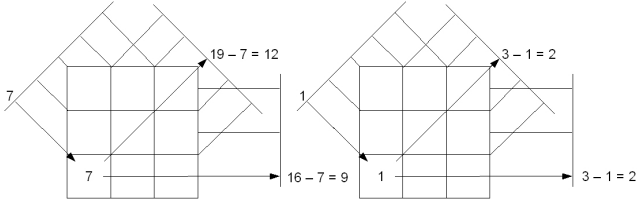


Figure 5. First step of the reconstruction : a projection line crosses only one pixel. Bin value is the pixel value. The pixel is reconstructed and its value is subtracted in the bins where it appears. Corresponding values in the M^t sinogram are decremented.

The reconstruction of the image is achieved when the total number of pixels has been treated. Since this process iteratively computes the image pixel by pixel, a $W \times H$ image is completely reconstructed in $W \times H$ steps. This algorithm is usually called Corner-Based Inversion (CBI). Because of the regular sampling, this algorithm is exact (in the sense that the reconstructed image is equal to the original one) if the sinogram is not noisy and the projection set follows the Katz criterion.

2.4 Spline Mojette Transform

The previous Dirac-Mojette transform uses the Dirac interpolator to select on each bin the crossed-on-center pixels. For instance in the figure 6, the two grey pixels give the bin valued 13. Notice that these pixels do not form a discrete line. The Spline-Mojette transform [6] has been developed to allow the bins to follow discrete lines. So, all the pixels crossed by a bin line are considered even if they are not centered. Spline-Mojette bins can be determined from Dirac-Mojette one's.

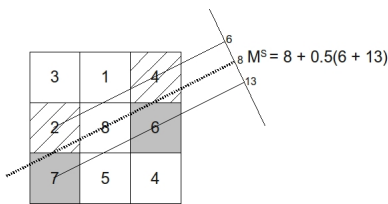


Figure 6. From the Dirac-Mojette to the Spline-Mojette acquisition.

Indeed on the figure 6, the central Dirac-Mojette bin is only composed of the central pixel. However, the corresponding line crosses grey and hatched pixels. Hatched (*resp.* grey) pixels define previous (*resp.* next) bin in the Mojette projection. Consequently, the Spline-Mojette value $M_{p,q}^s(b)$ can be expressed as a linear

combination of Mojette values [13] :

$$M_{p,q}^s(b) = \sum_{b_i=1}^{N_\rho(p,q)} \alpha_{p,q}(b, b_i) M_{p,q}(b_i) \quad (8)$$

where α is the Spline coefficient between two bins b and b_i [19].

The Spline-Mojette transform computes discrete line values from Dirac-Mojette bins. This process gives an acquisition equivalent to a discrete and finite Radon transform following specific acquisition angles [15]. In such a case, the projection line geometry is closer to continuous X-Ray attenuation obtained with a CT-scan acquisition. From Spline-Mojette values, Dirac-Mojette bins are fast recovered using a triangular system resolution [13] or a deconvolution.

2.5 CBI-Spline reconstruction

Another reconstruction approach from a Spline-Mojette acquisition consists in an adjustment of the CBI algorithm to the Spline interpolator. Then, $M_{p,q}^t(b)$ represents the number of crossed pixels according to the Spline geometry (i.e. $\{(i, j) \in I / \alpha_{p,q}(b, ip - jq) \neq 0\}$). For instance, the scheme 7(a) shows $M_{p,q}^s(b)$ and $M_{p,q}^t(b)$ values for the projection $(2, 1)$. From the M^t sinogram, we can find a univoque correspondence. Contrary to the previous algorithm, it is not necessary with a pixel crossed on the center. In this case, the contribution is done by the Spline weighting. For instance on the scheme 7(a), there is a univoque correspondence between the bin on the top and the hatched pixel, with a contribution 0.5. The pixel is then reconstructed according to its contribution as it is shown on the figure 7(b). Afterwards, the updates are processed on all the bins crossing the pixel according to their corresponding contributions (c.f. figure 7(c)). Update reveals a new correspondence. Then, like the previous algorithm, this one reconstructs directly the image pixel by pixel from a Spline-Mojette sinogram. Notice that whatever the Spline-Mojette reconstruction used, the result is exact in the sense that the reconstructed image is equivalent to the acquired one. In the following, we distinguish CBI-Dirac and CBI-Spline algorithms.

2.6 Advantages and Limitations of the Mojette reconstructions

The main advantage of Mojette reconstructions compared to usual methods is the robustness to the missing wedge effect. The reconstruction is exact even if the angular coverage of the projection set is strictly lesser than π . An example is given on the figure 8 with 4 projections distributed on $[0, \frac{\pi}{2}]$. First scheme represents the acquisition. Image 8(b) shows reconstruction of 4 pixels from the projection $(2, 1)$. Bin updates reveal two new univoque correspondences used (c.f. figure 8(c)) to reconstruct 2 more pixels. Finally, the 3 last pixels are reconstructed (cf. figure 8(d)). The reconstruction is exact whereas the acquisition angular coverage is only $\frac{\pi}{2}$.

The main drawback of CBI algorithms is their sensitivity to the noise in the projections. Since the projections are updated from a reconstructed pixel, the noise in the bins is propagating iteratively. The figure 9 shows the beginning of this propagation. Similarly, the reconstruction of Dirac-Mojette bins from noisy Spline-Mojette acquisition is ineffective using triangular system resolution.

Algorithms derived from usual tomography, such as the BFP-Mojette or iterative SART-Mojette have been developed [15] to overcome this limitation. They are not exact any more, but they achieve successfully a reconstruction from a noisy sinogram. They

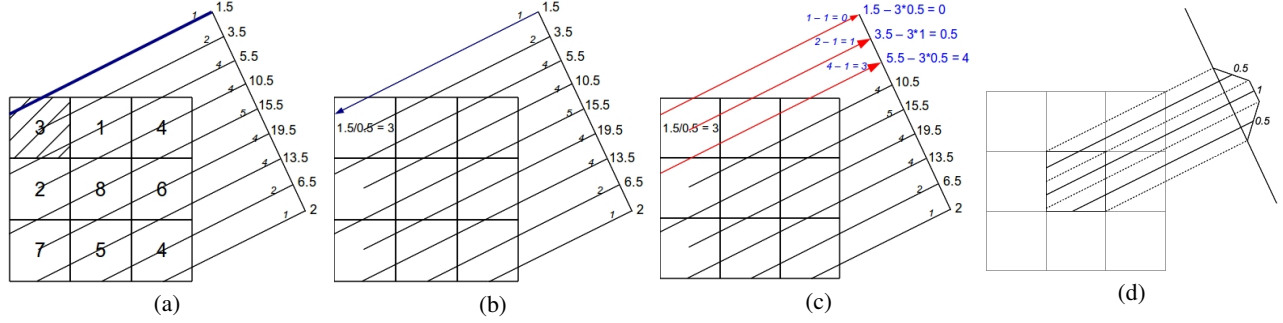


Figure 7. (a) Spline-Mojette acquisition of the projection (2,1) with the values of the associated unary sinogram. (b) Correspondance between a bin and a pixel and pixel reconstruction according to its Spline contribution into the bin. (c) Bin and unary sinogram updates according to the Spline weight of the reconstructed pixel. (d) Spline weighting of the bin crossing the central pixel for the projection (2, 1) used in this example.

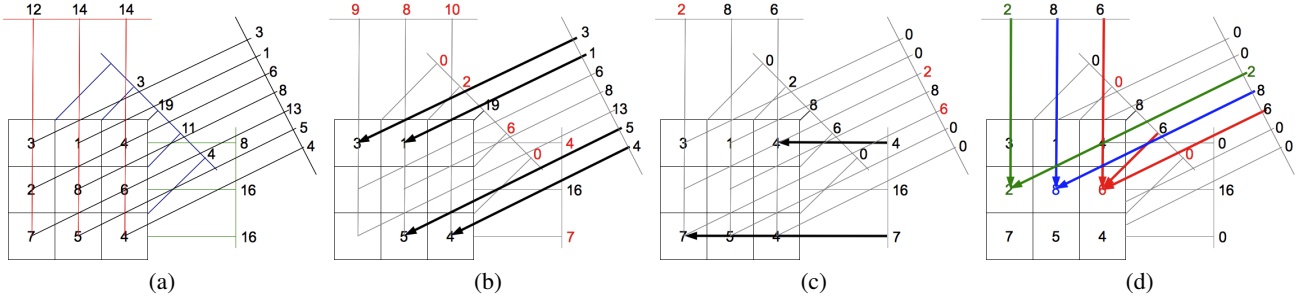


Figure 8. CBI reconstruction using 4 projections distributed on $[0, \frac{\pi}{2}]$.

can be applied as well as from a Dirac than from a Spline Mojette acquisition as it is shown on the figure 10. On the other hand, these methods are not robust to the missing wedge effect any more, except the Spline BFP-Mojette (cf. images on figure 11).

2.7 Goals

From the previous observations, it seems that the missing wedge effect is not only due to the unavailable projection set, but it is also a problem of data disassembling on existing projections. This data division is well ensured by Dirac bins (especially when using the CBI), but not anymore in Spline ones. Consequently, our goal in the following is to develop noise robust CBI [14] to observe the propagation of the missing wedge effect into the projections during the reconstruction process. Because this algorithm has to be launched from a Dirac-Mojette sinogram, we investigate on a noise robust inversion to compute an efficient projection data division giving Dirac bins from Spline ones. However, we also investigate on a noise robust CBI-Spline algorithm as an alternative solution.

3 Noise-robust CBI

In this section, we first develop a new method based on the CBI algorithm [14] which allows the reconstruction of an image from noisy Dirac-Mojette bins. Afterwards, we propose two solutions to reconstruct from a noisy Spline-Mojette sinogram. The first one is based on simulated annealing to recover the Dirac bins from a noisy Spline-Mojette or specific Radon acquisition. The second one is based on the CBI-Spline algorithm. It computes directly the image from the noisy Spline-Mojette acquisition.

3.1 New CBI algorithm for reconstruction from noisy projections

In this section, we develop new criteria about the pixel reconstruction and the bin update to lead on a new noise-robust CBI algorithm.

1) *Pixel reconstruction from multiple bin-pixel correspondences:* We can first observe that the greater the Farey series order is, the larger the projection number is. This redundancy of data increases the number of single bin-pixel correspondence available to reconstruct each pixel. For instance, a data redundancy example is exposed on the figure 8(d) (bold bin lines).

Let us denote P^k the set of not-reconstructed pixels at CBI iteration k . We denote $M_c(i, j)$ the ordered value set of bins $M_{p,q}(b) \geq 0$ such that the pixel $(i, j) \in P^k$ is crossed by the bin line (b, p, q) (i.e. $(i, j) \subset (b, p, q)$). Notice $M_{p,q}(b) \geq 0$ because a pixel value is positive. Then, a negative bin value is not significant even if some of associated pixels are not reconstructed. The bin set is defined by :

$$M_c(i, j) = \{M_{p_i, q_i}(b_i) \geq 0 / (i, j) \in P^k \wedge (i, j) \subset (b_i, p_i, q_i)\} \quad (9)$$

We denote $|M_c(i, j)|$ the set size. The reconstructed pixel value depends on the distribution chosen to exploit the bin value set. In our algorithm, we work with a Gaussian distribution instead of an average or median one because it gives a good estimate of the pixel value and it is not influenced by extrema. The pixel value is

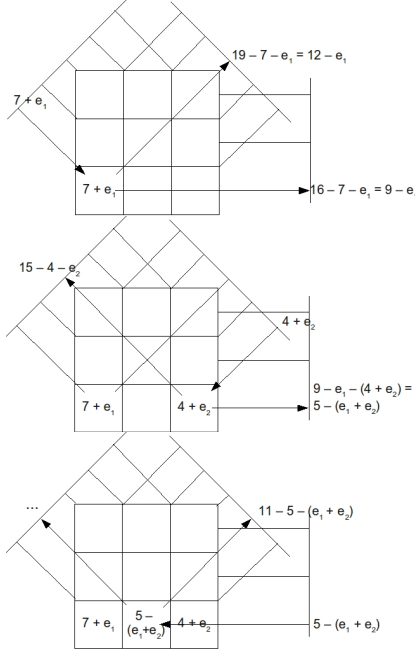


Figure 9. Iterative propagation of the noise from a bin to the others. The first reconstructed pixel is obtained from a bin containing an error e_1 . This error is introduced during bin updates in 2 other projections. A second pixel is reconstructed from a bin affected by an error e_2 . This error is in its turn inset into other bins. The third pixel is reconstructed with bottom right bin containing the two previous errors. Its erroneous value is deduced from the projections, and so on.

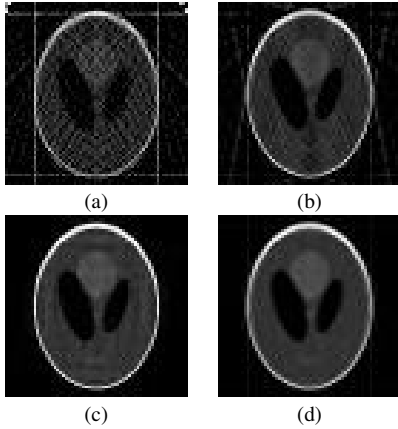


Figure 10. Reconstructed images using the BFP-Mojette from Dirac (a) and Spline (b) acquisition. Reconstructed images using the SART-Mojette from Dirac (c) and Spline (d) acquisition. Acquisition from a 64×64 pixel image with the set of projections given by the 5-order Farey series (minimum verifying the Katz criterion).

computed by :

$$I(i, j) = P(i, j, M) = \sum_{l=1}^{|M_c(i, j)|} e^{-\left(\frac{l - \lfloor \frac{|M_c(i, j)|}{2} \rfloor + \gamma}{\lfloor \frac{|M_c(i, j)|}{2} \rfloor}\right)^2} M_{p_l, q_l}(b_l) \quad (10)$$

where γ is a centering coefficient valued 0 by default.

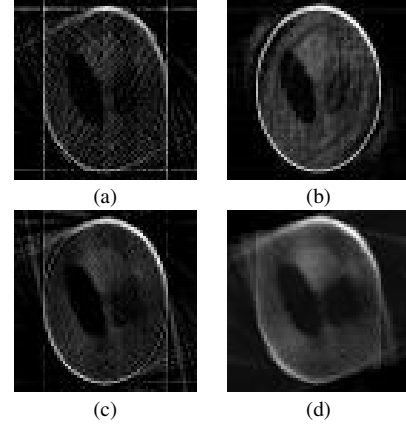


Figure 11. Missing wedge robustness of the BFP-Mojette and SART-Mojette algorithms. BFP-Mojette from Dirac (a) and Spline (b) acquisition. SART-Mojette from Dirac (c) and Spline (d) acquisition.

If all bins are negative whereas pixels to recover remain, the reconstruction is not achieved even if the Katz criterion is verified. In that case, the bin values are decreased too fast. In other words, the already reconstructed pixel intensities have been globally overvalued. To overcome this problem, the image reconstruction is restarted with a lesser pixel valuation. The γ coefficient is used to regulate this valuation.

2) *Pixel reconstruction from minimal erroneous bins*: The observation of the noise propagation also reveals that the more a bin is updated, the more its value is altered. From this noticing, we define $N_{p, q}^{up}(b)$ the number of incurred bin updates (by default, $N_{p, q}^{up}(b)$ is initialized with 0 value). Since a bin is updated each time an associated pixel is reconstructed, $N_{p, q}^{up}(b)$ corresponds to the number of already reconstructed pixels on the bin. The overall error on a reconstructible pixel (i, j) is denoted $E(i, j)$ and is defined by :

$$E(i, j) = \sum_{l=1}^{|M_c(i, j)|} N_{p_l, q_l}^{up}(b_l) \quad (11)$$

3) *Pixel selection*: The probability of a pixel being reconstructed accurately is proportional to the number of single bin-pixel correspondences and depends on the error $E(i, j)$. Consequently, we propose that the reconstructed pixel (i_k, j_k) at iteration k is the one with both the maximum correspondence number and the minimal error. These conditions are verified by :

$$(i_k, j_k) \in P^k / \begin{cases} |M_c(i_k, j_k)| = \max\{|M_c(i, j)|, (i, j) \in P^k\} \\ E(i_k, j_k) = \min\{E(i, j), (i, j) \in P^k\} \end{cases} \quad (12)$$

4) *Mollified bin-pixel correspondences*: Now the bin error is defined, we can introduce the exactness probability of a bin used to reconstruct a pixel at iteration k as :

$$p_{p, q}^k(b) = e^{-\frac{N_{p, q}^{up}(b)}{D_{p, q}(b)}} \quad (13)$$

where $D_{p, q}(b) = M_{p, q}^t(b)_{k=0}$ is the distance (in pixels) crossed by the projection line in the image. It corresponds to the initial value of $M_{p, q}^t(b)$. The probability is introduced in equation 10 to

mollify the bin importance for the reconstructed pixel according to its exactness. The overall pixel computation formula becomes :

$$I(i, j) = \sum_{l=1}^{|M_c(i, j)|} p_{p_l, q_l}^k(b_l) e^{-\left(\frac{|M_c(i, j)| + \gamma}{\frac{|M_c(i, j)|}{2}}\right)^2} M_{p_l, q_l}(b_l) \quad (14)$$

5) *Mollified bin updates:* In the original CBI, a bin value $M_{p, q}(b)$ is updated by $M_{p, q}(b) - I(i_k, j_k)$ when the associated pixel (i_k, j_k) is reconstructed. In the new algorithm, the bin update is mollified to reduce the noise effect and the risk that a reconstruction does not finish because all bins are negative. The bin update becomes :

$$M_{p, q}(b) = M_{p, q}(b) - \frac{I(i_k, j_k)}{Z(\gamma)} \quad (15)$$

where $Z(\gamma)$ is an attenuation coefficient depending on γ . If the reconstruction can not be achieved despite of this precaution, the γ coefficient is increased and the reconstruction process is reinitialized.

6) *Pixel update from final bin values:* In the original CBI algorithm, a bin is valued 0 if all the associated pixels are reconstructed. This property is not verified in our reconstruction because of the noise on the projections. This non-zero value can be re-injected into the image. By default, we can update uniformly each pixel associated with the considered bin. However, earlier a pixel is reconstructed, the more its value is accurate. As before with the correctness probability of bins, we define the correctness probability of a pixel according to its reconstruction rank k by :

$$p^k(i, j) = e^{-\frac{k}{N}} \quad (16)$$

Then, given a final bin value $M_{p, q}^k(b)$ at iteration k , the associated pixels are updated with :

$$I(i, j) = I(i, j) - \frac{p^k(i, j)}{\sum_{(i, j) \subset (b, p, q)} p^k(i, j)} M_{p, q}^k(b), \forall (i, j) \subset (b, p, q) \quad (17)$$

7) *The algorithm:* Considering the previous definitions, the new CBI performs as detailed in algorithm 1. This noise robust algorithm is denoted NRCBI-Dirac in the following.

3.2 From noisy Spline-Mojette to Dirac-Mojette bins

We develop now a new method to reconstruct the Mojette bins from noisy Spline-Mojette data. The process is an iterative reconstruction in h which approximates the bin value $M_{p, q}^{h+1}(b)$ at iteration $h+1$ by successive comparisons of original Spline-Mojette values $M_{p, q}^s(b)$ and recomputed $M_{p, q}^{s, h}(b)$ (performed from M^h). The bin update step is then computed as follows :

$$M_{p, q}^{h+1}(b) = M_{p, q}^h(b) + Esp_{p, q}^h(b) \quad (18)$$

where $Esp_{p, q}^h(b)$ is defined by a Simulated Annealing (SA) step. In the algebraic reconstruction, the unpenalized update value is usually defined by :

$$Esp_{p, q}^{h, 0}(b) = \frac{\sum_{b_i=1}^{N_\rho(p, q)} \alpha_{p, q}(b, b_i) (M_{p, q}^s(b_i) - M_{p, q}^{s, h}(b_i))}{\sum_{b_i=1}^{N_\rho(p, q)} \alpha_{p, q}(b, b_i)} \quad (19)$$

where $M_{p, q}^{s, h}(b_i) = \sum_{b_j=1}^{N_\rho(p, q)} \alpha_{p, q}(b_i, b_j) M_{p, q}^h(b_j)$ is the recomputed Spline value from bins obtained at previous iteration.

Algorithm 1: $CBI_{noise}(M)$

```

1  $\gamma \leftarrow 0$ ;
2  $k \leftarrow 0$ ;
3  $P^k = \{(i, j) / (i, j) \in I\}$ ;
4  $\forall (b_l, p_l, q_l) \in M, N_{p_l, q_l}^{up}(b_l) \leftarrow 0$ ;
5 while  $P^k \neq \emptyset$  do
6   find  $(i_k, j_k)$  using criterion 12;
7   if  $(i_k, j_k) \neq NULL$  then
8      $I(i_k, j_k) = P(i, j, M)$  (formula 14);
9      $P^k \leftarrow P^k - (i_k, j_k)$ ;
10  end
11 else
12    $\gamma \leftarrow \gamma + 1$ ;
13   restart from line 2;
14 end
15 foreach  $(b_l, p_l, q_l) \in M_c(i_k, j_k)$  do
16   update  $M_{p_l, q_l}(b_l)$  with equation 12;
17   increase  $N_{p_l, q_l}^{up}(b_l)$  and decrease  $M_{p_l, q_l}^t(b_l)$ ;
18   if  $N_{p_l, q_l}(b_l) = 0 \wedge M_{p_l, q_l}(b_l) \neq 0$  then
19     update all  $(i, j) \subset (b_l, p_l, q_l)$  (formula 17)
20   end
21 end
22 end
23 return  $I$ ;

```

We now define the penalized update value as :

$$Esp_{p, q}^{h, N}(b) = Esp_{p, q}^{h, 0}(b) + \frac{P(Esp_{p, q}^{h, 0}(b))}{F(h+1)} \quad (20)$$

where $P(x)$ returns a random value in $[-\frac{x}{2}, \frac{x}{2}]$, and $F(x)$ is an increasing function whose ensures that the maximal error applied decreases when the iteration step increases.

Following a simulated annealing procedure, the overall update step is defined by :

$$Esp_{p, q}^h(b) = \begin{cases} Esp_{p, q}^{h, 0}(b) & \text{if } Esp_{p, q}^{h, 0}(b) < Esp_{p, q}^{h, N}(b) \\ Esp_{p, q}^{h, N}(b) & \text{if } \begin{cases} Esp_{p, q}^{h, 0}(b) > Esp_{p, q}^{h, N}(b) \\ p < e^{-\frac{h}{h_{max}}} \end{cases} \\ 0 & \text{else.} \end{cases} \quad (21)$$

where p is randomly chosen in $[0, 1]$, and h_{max} is defined as the maximum iteration *Temperature*.

We denote $E^h = \sum_b |M_{p, q}^s(b) - M_{p, q}^{s, h}(b)|$ the error between the original and recomputed Spline projection at iteration h . The iterative process is stopped when $E^h - E^{h+1} \leq \epsilon$, where ϵ is a given parameter. This iterative process allows the computation of each bin value and finally gives an approximation of the Dirac-Mojette projections. Moreover, the final error E^h can be introduced into the NRCBI-Dirac algorithm as initial bin error value $N_{p, q}^{up}(b)$.

3.3 Investigation about a noise robust CBI-Spline algorithm

Now, we adjust the noise robust CBI algorithm to the Spline geometry. The pixel selection performs similarly, i.e. from the

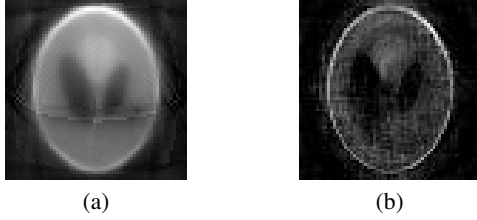


Figure 12. Reconstructions from noisy Spline-Mojette sinogram. Image obtained with the NRCBI-Spline method (a). Image obtained with the SA + NRCBI-Dirac algorithm (b).

minimal error and maximum bin set size. The bin set is obtained by taking into account the Spline contribution of each bin crossing a pixel. Similarly, the bin updates are not limited to the bins crossing the pixel center. All the bins going through the pixel (according to their corresponding Spline weights) are updated.

Moreover, the final Spline-Mojette bin value is re-injected in all the traversed pixels, according to their contributions. Note $t(p, q)$ the sum of Spline contributions of the projection (p, q) . For instance, $t(2, 1) = 0.5 + 1 + 0.5 = 2$ (cf. figure 7(d)). When the bin l is at end of use on the projection $(2, 1)$, we distribute $\frac{0.5}{t(2,1)} M_{2,1}^s(l)$ on the pixels crossed by the bins $l - 1$ and $l + 1$ (because they are crossed by l with the contribution 0.5). Finally, we distribute the final error $\frac{1}{t(2,1)} M_{2,1}^s(l)$ between each pixel crossed on the center by the bin l . This method is denoted NRCBI-Spline in the following.

3.4 SA+NRCBI-Dirac or NRCBI-Spline ?

Even if the NRCBI-Spline method is theoretically close to the NRCBI-Dirac algorithm, it performs a number of bin update very larger than the previous one. Consequently, the residual error on the bins is larger. It can smooth the image when it is re-injected on the pixels. Inversely, SA + NRCBI-Dirac suffers from the errors induced by the two steps of the reconstruction. For instance, image shown on the figure 12(a) is reconstructed with the NRCBI-Spline algorithm from a noisy sinogram whereas the image 12(b) is obtained using the SA + NRCBI-Dirac algorithm. We recall that the usual triangular resolution system + CBI-Dirac algorithm or the CBI-Spline method give the same and exact reconstruction when it is applied for a not noisy sinogram. In the presence of noise, the new both methods have to be studied and discussed because their results are not equivalent any more.

4 Results and Discussion

In this section, we detail the reconstruction results obtained with the algorithms developed above. They are tested on the well-known Lena image and on the synthetic Shepp-Logan [16] phantom (which is an usual test image in tomography). From the original images sized 64×64 , the Mojette (or Spline-Mojette) sinogram M is acquired using different Farey series from the order 5 (minimum projection set following the Katz criterion). Each sinogram is biased with an additive uniform noise whose value $B_{p,q}(b)$ is randomly chosen in interval $[-2.5\% M_{max}, 2.5\% M_{max}]$, where $M_{max} = \max\{M_{p,q}(b), (b, p, q) \in M\}$.

The reconstructed image properties are compared to the original one using the Structural SIMilarity (SSIM) criterion [21] :

$$SSIM(I, J) = l(I, J) \cdot c(I, J) \cdot r(I, J) \quad (22)$$

where $0 \leq l(I, J) \leq 1$ (*resp.* $0 \leq c(I, J) \leq 1$) is the global intensity (*resp.* contrast) comparison between two images I and J , and $0 \leq r(I, J) \leq 1$ is the correlation coefficient. $0 \leq SSIM(I, J) \leq 1$ gives the quality rate of the reconstruction. The closer the SSIM value is to 1, the better the reconstruction quality is. Moreover, noise robustness is measured with signal to noise ratio (SNR). It is expressed in dB and represents signal loss.

4.1 Reconstruction from noisy Dirac-Mojette acquisition

We first show the results obtained with the NRCBI-Dirac algorithm for reconstructing an image from noisy Mojette bins. Resulted images and comparisons are detailed on the table I. \overline{CBI} value denotes the average number of bin-pixel correspondences used to reconstruct a pixel. Results are compared with the efficient and noise robust SART-Mojette method.

Since the standard CBI resolution diverges, the final reconstruction step is not reached. Conversely with the new algorithm, the reconstruction is achieved when the Katz criterion is verified. The reconstruction quality increases with the Farey series order, i.e. with the number of projections. From the 5-order Farey series results, we denote the importance of data redundancy to achieve a reconstruction with a great quality rate. Indeed, the SSIM obtained to reconstruct the simple Shepp-Logan phantom is up than 0.8, but Lena only gives a $SSIM = 0.6$.

From the 7-order, the acquisition contains sufficient data density, i.e. a sufficient single bin-pixel correspondence number to reconstruct each pixel accurately. The Lena image quality becomes better than 0.8. The Shepp-Logan image quality is up to 0.95 when the projection number becomes large (from the 9-order Farey series). The SNR of the Shepp-Logan increases significantly with the Farey series order. Since this phantom contains a lot of uniform regions, their intensities are properly averaged through the large density data on the projections. This is the reason why the signal loss goes from -2.25 to -0.78 when the Farey series order increases from 5 to 10. Conversely, even if the SNR of images containing more details (Lena for instance) seems to be improved with the projection number, its value is quasi-stabilized from Farey order 7. So, we can globally conclude that the SNR remains constant whatever the projection number.

Finally, we denote that the reconstruction is not competitive with the results obtained by the Dirac SART-Mojette reconstruction for the Lena image. Inversely on Shepp-Logan reconstruction, the images are as well as recovered when the number of projections becomes large.

4.2 Reconstruction from Noisy Spline-Mojette acquisition

Now, we detail the reconstruction results obtained from a noisy Spline-Mojette acquisition. The protocol test is similar as above, except that the noise is applied on the Spline sinogram. First, the images are computed from this one using the SA + NRCBI-Dirac method. Note that the noise on the Mojette bins is then due to the noise applied on Spline acquisition enforced by the SA approximations. Second, the images are computed using the NRCBI-Spline algorithm. The resulted images and corresponding comparison values are given on the table II.

The image quality increases between Farey series of orders 5 and 7. Afterwards, contrary to CBI-Dirac results, the quality decreases when the Farey series order increases. It is particularly noticeable












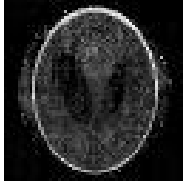








Farey order Projections \overline{CBI}	5 40 1.71	7 72 5.88	9 112 11.86	10 128 14.83	
					NRCBI-Dirac
SSIM SNR	0.609 -2.93	0.813 -2.07	0.837 -2.07	0.841 -2.04	
					Dirac SART-Mojette
SSIM SNR	0.963 -0.47	0.993 1.19	0.993 1.27	0.993 1.01	
					NRCBI-Dirac
SSIM SNR	0.885 -2.25	0.966 -1.10	0.964 -1.09	0.974 -0.78	
					Dirac SART-Mojette
SSIM SNR	0.993 0.44	0.999 2.67	0.999 2.93	0.999 2.40	

Table I

IMAGES RECONSTRUCTED WITH NOISE ROBUST CBI AND SART-MOJETTE FROM DIRAC-MOJETTE SINOGRAMS ALTERED BY AN ADDITIVE AND UNIFORM NOISE. ACQUISITIONS USING DIFFERENT FAREY SERIES ORDER (FROM MINIMAL ORDER 5 TO ENSURE THE KATZ CRITERION). THE CORRESPONDING PROJECTION NUMBER AND AVERAGE NUMBER OF CORRESPONDENCES (\overline{CBI}) ARE GIVEN. THE STRUCTURAL SIMILARITY RATE SSIM AND THE SIGNAL LOSS EXPRESSED BY THE SNR ARE DETAILED.

on the Lena results whatever the method used. However, the SSIM converges when the Farey series order becomes greater than 9. It is close to 0.65 (Lena) and 0.82 (Shepp-Logan) using the SA + NRCBI-Dirac method whereas it is close to 0.57 (Lena) and 0.52 (Shepp-Logan) using the NRCBI-Spline algorithm. Then, the image quality is better using the first method. Moreover, image reconstruction is not stabilized with the NRCBI-Spline algorithm as it is noticeable on the Shepp-Logan result using 9-order Farey series.

On the other hand, the SNR is improved on the Shepp-Logan phantom results whatever the method whereas it decreases with the second method on Lena results. The NRCBI-Spline algorithm reinjects a too large part of the final bin error. Then, it acts as a smoothing on the image and it deteriorates the SNR. The bin update, necessary in the NRCBI algorithms to contain the error,

is in fact too important here. It finally deteriorates image quality. However, it can not be ousted otherwise the reconstruction fails. Let us consider now the SA + NRCBI-Dirac SNR results. The “noise” implied by the SA resolution still gives a smoothness of bin values and finally acts as a low pass filter on the images.

Globally, the results are fuzzier than the ones obtained from a Mojette acquisition (whatever the method) and corresponding SSIM and SNR are worse. Then, the both new methods are not competitive with the Spline SART-Mojette method for now.

4.3 Reconstruction from Spline-Mojette acquisition with missing wedge

Now, we observe the reconstruction of a Spline-Mojette acquisition with missing wedge. Note that if the Spline-Mojette sinogram is noise free, we can recover the Dirac bins from the spline ones using a triangular linear system resolution [13]. In a such case, the



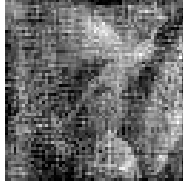

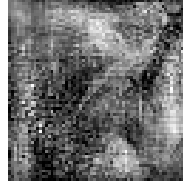











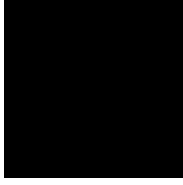
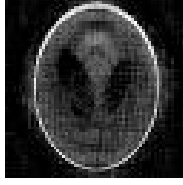
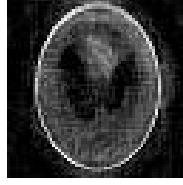
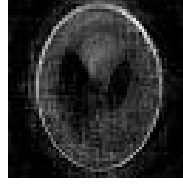

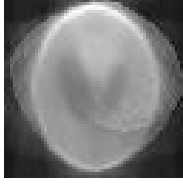
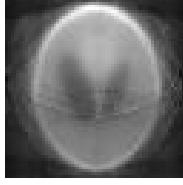

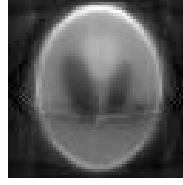





Farey order	5	7	9	10	
					SA + NRCBI-Dirac
SSIM SNR	0.371 -3.56	0.693 -2.48	0.656 -2.70	0.651 -2.65	
					NRCBI-Spline
SSIM SNR	0.68 -2.80	0.64 -3.31	0.58 -3.57	0.574 -3.60	
					Spline SART-Mojette
SSIM SNR	0.950 -0.68	0.979 -0.16	0.988 -0.64	0.991 -0.77	
					SA + NRCBI-Dirac
SSIM SNR	0.000 -4.38	0.892 -2.29	0.839 -2.76	0.821 -2.60	
					NRCBI-Spline
SSIM SNR	0.372 -4.44	0.453 -5.16	0.500 -4.71	0.513 -3.61	
					Spline SART-Mojette
SSIM SNR	0.994 0.53	0.999 2.43	0.999 3.05	0.999 2.66	

Table II

IMAGES RECONSTRUCTED FROM NOISY SPLINE-MOJETTE SINOGRAM. SA + NRCBI-DIRAC RESULTS : THE MOJETTE BINS ARE FIRST RECOVERED USING SA ALGORITHM AND THE NOISE-ROBUST CBI IS LAUNCHED. NRCBI-SPLINE RESULTS ARE OBTAINED DIRECTLY FROM THE NOISY SPLINE-MOJETTE SINOGRAM. THE SSIM AND SNR ARE DETAILED TO ESTIMATE THE GLOBAL RECONSTRUCTION QUALITY. RESULTS ARE COMPARED TO THE SPLINE SART-MOJETTE RECONSTRUCTION.

computed Mojette bins are exact. The overall Mojette sinogram is then noise free. Reconstruction with usual CBI algorithm is achieved successfully (exact reconstruction) if the projection set follows the Katz criterion.

For instance, considering an image sized 64×64 pixels, the 10-order Farey series gives 128 projections between 0 and π . If we delete the projections between $\frac{2}{3}\pi$ and π , the 85 remaining projections still follow the Katz criterion. If the sinogram is not noisy, the reconstruction is achieved successfully.

In the same condition with a noisy sinogram, the usual protocol fails, and reconstruction using Spline SART-Mojette gives deformation in the regions of the image (cf. results on figure 13(a)). The image reconstructed with the SA + the NRCBI-Dirac method is given on figure 13(b). We can denote that the reconstruction is geometrically more accurate - especially the external contour of the head phantom - even if it is more noisy than the SART-Mojette one. Even if it can not be used at once to reconstruct from incomplete acquisition, it could be a solution to compute the initial image used by iterative methods. Inversely, the NRCBI-Spline method is not robust to the missing wedge effect anymore because deformations appear in the result (cf. figure 13(c)). These deformations are generated by the non-uniform and too large pixel correction using final bin values (it is not uniform in the sense that final bin error is not covering uniformly the image between 0 and π).

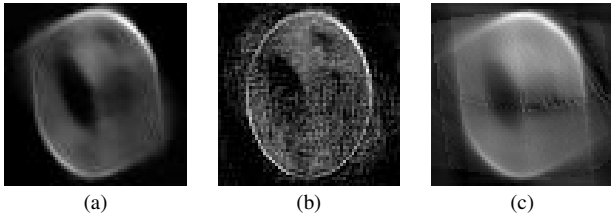


Figure 13. Reconstructed images using the SART-Mojette (a), SA + NRCBI-Dirac (b) and NRCBI-Spline (c) algorithms from an acquisition with missing projection set.

4.4 Reconstruction from a real acquisition

Because the new algorithms perform image reconstruction from noisy sinogram, we can investigate the reconstruction from an usual acquisition (for instance, a sinogram similar to the figure 1(b)). In a such case, the Mojette sinogram is obtained by interpolation from the real sinogram to map the uniform acquisition (constant angular step $\delta\theta$ and constant radial step $\delta\rho$) into Spline-Mojette bins. Here, the Farey series giving the projection number the closest to the number of acquired angles is chosen. Afterwards, a radial (along the samples) and angular (along the projections) interpolation is performed between acquisition and Spline-Mojette bins. Finally, the SA + NRCBI-Dirac or the NRCBI-Spline algorithms are launched.

For instance, the image 14(a) is obtained from the usual sinogram 1(b). First, it is interpolated into a Spline-Mojette sinogram and second, the SA + NRCBI-Dirac is performed. Similarly, the image 14(b) is obtained using the NRCBI-Spline method.

Let us consider now the reconstruction from a sinogram with missing wedge. For instance, the image 14(c) is obtained from the sinogram 3(a). Despite the noise into the image, data deformation are visible whereas the algorithm used is robust the missing wedge

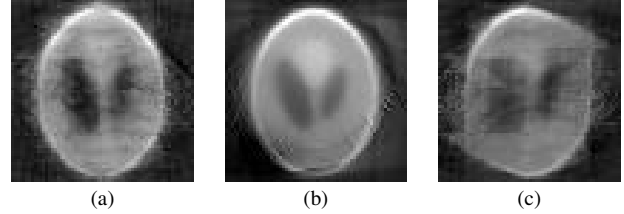


Figure 14. Reconstruction from a real acquisition using a radial/angular interpolation between the acquired sinogram and the Spline-Mojette bins. (a) Reconstruction without missing wedge from sinogram 1(b). (b) Reconstruction with missing wedge from sinogram 3(a).

(cf. results on the figure 13). NRCBI-Spline algorithm is not considered anymore because we have already highlighted that it is sensitive to the missing wedge.

Consequently, the interpolation step reveals an alternative issue to the missing wedge effect. Indeed, image deformations are necessarily due to the acquisition and interpolation steps because they are the only ones that differ from the previous protocol. In other words, deformations are not due to the missing wedge but are the consequence of poor accuracy on existing projections. This poor accuracy can be the consequence of both the acquisition sampling (which is not sufficient) and the interpolation (which not correctly separates projection data into the bins).

5 Conclusion and Perspectives

The missing wedge effect is observed in usual tomography when a set of projections is not available along several angles. It implies deformations in the reconstructed image. The investigation proposed in this paper focuses on a discrete geometry approach based on the Mojette transform. This study highlighted that the missing wedge effect is not only due to the missing projections but also to a leak of precision in the existing projections. The Dirac-Mojette transform is not sensitive to the missing wedge effect because projection data are already well separated. However, this geometry is not compatible with usual tomography. Spline-Mojette is closer to an usual acquisition geometry, and we have developed new noise robust CBI algorithms in order to apply them from noisy Mojette or real acquisitions. Unfortunately, the reconstructions are not as competitive as other noise robust algorithms such as SART-Mojette.

Indeed, the CBI algorithms explained in this paper allow an inversion from noisy projections. The used sinogram can be a noisy Mojette one as well as an interpolated Radon acquisition. According to the results obtained, the developed algorithms compute images efficiently but still need to be optimized (especially the NRCBI-Spline method). We first have to model the noise and its propagation between the projections to improve and to regulate the pixel valuation. A pixel computation more efficient than the Gaussian distribution has to be developed according to the noise model. Using this specific technique, we are going to observe the evolution of data in the sinogram step by step during the reconstruction. This tool could be used to locate for instance anomalies during the reconstruction (especially those generated by the missing wedge).

Moreover, the SA algorithm has to be improved for the NRCBI to be used in tomography. The optimization of this part of the

algorithm is an essential goal, especially because it smoothes the Mojette bins and finally affects the reconstructed image quality. This remark is also available for the NRCBI-Spline algorithm, proposed as an alternative solution of the SA + NRCBI method (even if it is noise and missing wedge sensitive for now). More particularly, SA is the essential algorithm step allowing the projection data division. The quality of this division seems to be a solution to the missing wedge problem. This specific use has to be developed and results have to be compared with those obtained by other methods which deal with missing wedge effect (such as dual-axis algorithms [2] or wavelet-based reconstruction). Finally, adjusting the usual acquisition geometry (in Radon transform) to the specific Mojette one without projection detail loss (due to the radial/angular interpolation) will be a main goal in our future works.

References

- [1] A. H. Andersen and A. C. Kak. Simultaneous algebraic reconstruction technique (SART) : A superior implementation of the ART algorithm. *Ultrasonic Imaging*, 6:81–94, 1984.
- [2] Ilke Arslan, Jenna R. Tong, and Paul A. Midgley. Reducing the missing wedge: High-resolution dual axis tomography of inorganic materials. *Ultramicroscopy*, 106(11-12):994–1000, 2006. Proceedings of the International Workshop on Enhanced Data Generated by Electrons.
- [3] Thomas Frese, Ned C. Rouze, Charles A. Bouman, Ken Sauer, and Gary D. Hutchins. Quantitative Comparison of BFP, EM and Bayesian Reconstruction Algorithms for the IndyPET Scanner. *IEEE Transactions On Medical Imaging*, 22(2):258 – 276, February 2003.
- [4] Richard Gordon. A Tutorial on ART. *IEEE Transactions on Nuclear Science*, 21(3):78 – 93, June 1974.
- [5] Huaiqun Guan and Richard Gordon. Computed tomography using algebraic reconstruction techniques (ARTs) with different projection access schemes : a comparison study under practical situations. *Physics in Medicine and Biology*, 41:1727 – 1743, 1996.
- [6] Jean-Pierre Guédon. *The Mojette Transform : Theory and Applications*. ISTE-Wiley, 2009.
- [7] Jean Pierre Guédon and Nicolas Normand. Spline Mojette Transform : Applications in Tomography and Communications. *EUSIPCO*, 3:271–274, 2002.
- [8] Jean-Pierre Guédon and Nicolas Normand. The Mojette Transform: The First Ten Years. pages 79–91, 2005.
- [9] Ming Jiang and Ge Wang. Convergence of the Simultaneous Algebraic Reconstruction Technique (SART). *IEEE Transactions On Image Processing*, 12(8):957 – 961, August 2003.
- [10] Myron Bernard Katz. Questions of Uniqueness and Resolution in Reconstruction from Projections. *Lecture Notes in Biomathematics*, 1978. Springer-Verlag New York.
- [11] L. Kaufman. Implementing and accelerating the EM algorithm for positron emission tomography. *IEEE Transactions on Medical Imaging*, 6:37 – 51, 1987.
- [12] Johann Radon. Über die Bestimmung von Funktionen durch ihre Integralwerte langs gewisser Mannigfaltigkeiten. *Ber. Ver. Sachs. Akad. Wiss. Leipzig, Math-Phys. Kl*, 69:262–277, April 1917. In German. An english translation can be found in S. R. Deans : *The Radon Transform and Some of Its Applications*.
- [13] Benoit Recur, Pascal Desbarats, and Jean-Philippe Domenger. Radon and Mojette Projections’ Equivalence for Tomographic Reconstruction using Linear Systems. *WSCG 2008 Communication Papers*, pages 191–198, 2008.
- [14] Benoit Recur, Pascal Desbarats, and Jean-Philippe Domenger. Mojette Reconstruction from Noisy Projections. *IEEE International Conference on Image Processing Theory, Tools and Applications (IPTA)*, pages 201–206, July 2010.
- [15] Myriam Servieres, Nicolas Normand, Jean Pierre Guédon, and Yves Bizais. The Mojette Transform: Discrete Angles for Tomography. 20:587–606, 2005.
- [16] L. Shepp and B. Logan. The Fourier Reconstruction of a Head Section. *IEEE Transactions in Nuclear Science*, 21(2):21 – 43, 1974.
- [17] L. A. Shepp and Y. Vardi. Maximum Likelihood Reconstruction for Emission Tomography. *IEEE Transactions on Medical Imaging*, 1(2):113 – 122, October 1982.
- [18] Peter Toft. *The Radon Transform : Theory and Implementation*. PhD thesis, Department of Mathematical Modelling, Section for Digital Signal Processing, Technical University of Denmark, 1996.
- [19] M. Unser, A. Aldroubi, and M. Eden. B-Spline signal processing: Part I—Theory. *IEEE Transactions on Signal Processing*, 41(2):821–833, February 1993. IEEE Signal Processing Society’s 1995 best paper award.
- [20] M. Unser, A. Aldroubi, and M. Eden. B-Spline signal processing: Part II—Efficient design and applications. *IEEE Transactions on Signal Processing*, 41(2):834–848, February 1993.
- [21] Zhou Wang, Alan C. Bovik, Hamid R. Sheikh, and Eero P. Simoncelli. Image quality assessment : From error visibility to structural similarity. *IEEE Transactions on Image Processing*, 13, April 2004.